


Electronic and vibrational excitations on the surface of the three-dimensional topological insulator $\text{Bi}_2\text{Te}_{3-x}\text{Se}_x$ ($x = 0, 2, 3$)

A. C. Lee ^{1,*}, H.-H. Kung ^{1,†}, Xueyun Wang ^{1,2}, S.-W. Cheong ^{1,2} and G. Blumberg ^{1,3,‡}

¹*Department of Physics & Astronomy, Rutgers University, Piscataway, New Jersey 08854, USA*

²*Rutgers Center for Emergent Materials, Rutgers University, Piscataway, New Jersey 08854, USA*

³*National Institute of Chemical Physics and Biophysics, 12618 Tallinn, Estonia*

 (Received 27 May 2023; revised 25 September 2023; accepted 3 October 2023; published 1 November 2023)

We study surface states in the three-dimensional topological insulators $\text{Bi}_2\text{Te}_{3-x}\text{Se}_x$ ($x = 0, 2, 3$) by polarization resolved resonant Raman spectroscopy. By tracking the spectral intensity of the surface phonon modes with respect to the incident photon energy, we show that the surface phonons are qualitatively similar to their bulk counterparts. Using the resonant Raman excitation profile, we estimated the energy gaps between the surface conduction bands and the bulk conduction bands. In addition, we selectively excite the surface-to-bulk electronic continuum near the Fermi energy in Bi_2Se_3 to determine the strength of Fano interaction between the most prominent surface phonon and the surface-to-bulk continuum.

DOI: [10.1103/PhysRevB.108.174301](https://doi.org/10.1103/PhysRevB.108.174301)

I. INTRODUCTION

Three-dimensional topological insulators (3DTIs) are materials that contain gapless, Dirac-like electronic surface states [1–3] that are topologically protected against elastic scattering by nonmagnetic defects [4] making them attractive candidates to the application of devices where coherent spin-polarized transport is desired [5]. Given that the electronic surface states in 3DTIs are confined to the topmost unit cells [6], complete understanding of the lattice dynamics interacting with the surface states is critical. This knowledge is essential not only because the abrupt surface termination in materials can radically alter the crystal structure and electronic properties at the surface, but also because inelastic scattering from surface to bulk electronic states via phonons is expected to be the dominant low-energy scattering mechanism at room temperature [7]. For these reasons, we investigated the surface phonons in the 3DTIs $\text{Bi}_2\text{Te}_{3-x}\text{Se}_x$ ($x = 0, 2, 3$) using polarization-resolved resonant Raman spectroscopy to elucidate their interaction with the electronic states.

The bismuth-based 3DTIs $\text{Bi}_2\text{Te}_{3-x}\text{Se}_x$ are extensively studied topological insulator systems due to their stoichiometry, large bulk band gap, and simple surface spectrum. $\text{Bi}_2\text{Te}_{3-x}\text{Se}_x$ are composed of quintuple layers (QL) of covalently bonded Bi, Te, and Se atoms stacked along the c axis [8] with D_{3d} ($R\bar{3}m$) point group symmetry [8]. The symmetry of the topmost QL is reduced from the 3D $R\bar{3}m$ group to the two-dimensional (2D) C_{6v} ($P6mm$) wallpaper group. The QL are weakly bound together by van der Waals forces resulting in a quasi-2D electronic band structure [9–11]. The principal bulk

band gap is found at the Γ point. The lowest bulk conduction band is denoted as CB0. The highest occupied Dirac-cone, $SS1$, is composed of electronic surface states, and lies within the principal bulk band gap, where the bands cross at the $\bar{\Gamma}$ point [10–12]. There is also an unoccupied Dirac cone that lies between the second- and third-lowest bulk conduction bands [13].

In this work, we apply the polarization-resolved resonant Raman excitation profile (RREP) spectroscopy of the bulk and surface phonon modes in the bismuth based topological insulators $\text{Bi}_2\text{Te}_{3-x}\text{Se}_x$ to study excitations between the bulk and surface bands. The surface phonons were identified and characterized by using polarization-resolved measurements at the incident photon energies that maximize the surface phonon intensity. We detect the relative energy gaps between the surface bands by analyzing the intensity of the phonon modes as a function of incident photon energy. We selectively excite the lowest energy electron-hole excitation continuum due to transitions from surface to bulk electronic states that interacts with the surface phonons. For Bi_2Se_3 , by analyzing the interference Fano lineshape of the surface phonons with the continuum as a function of excitation energy, we establish the electron-phonon coupling strength between the surface phonons and the electronic surface states near the Fermi energy. This work also extends the earlier studies of surface phonons in Bi_2Se_3 [14] and Bi_2Te_3 [15] as it includes resonant Raman enhancement effects, as well as results for $\text{Bi}_2\text{Te}_2\text{Se}$.

II. EXPERIMENTAL DETAILS

Single crystals of $\text{Bi}_2\text{Te}_{3-x}\text{Se}_x$ were grown by the modified Bridgman technique [16]. Although the chemical potential in ideal topological insulators rests at the intersection point of the Dirac cones within the principal bulk band gap, the presence of natural defects typically raises the chemical potential into the upper Dirac cone and CB0 [16,17], thus, the lowest

*aclee@physics.rutgers.edu

†Present address: Quantum Matter Institute, University of British Columbia, Vancouver, BC V6T 1Z4, Canada.

‡girsh@physics.rutgers.edu

TABLE I. The Raman selection rules in the bulk and on the surface of $\text{Bi}_2\text{Te}_{3-x}\text{Se}_x$ ($x = 0, 2, 3$).

Scattering Geometry	Bulk (D_{3d})	Surface (C_{6v})
XX	$A_{1g} + E_g$	$A_1 + E$
XY	$A_{2g} + E_g$	$A_2 + E$
RR	$A_{1g} + A_{2g}$	$A_1 + A_2$
RL	$2E_g$	$2E$

conduction bands for all samples are assumed to be occupied. The chemical potential of the Bi_2Se_3 samples grown for this study were determined by scanning tunneling spectroscopy to cross approximately 150 meV above the Dirac point of the principal surface band [16] and was later confirmed also by optical studies [18,19]. All samples were cleaved in a N_2 -rich glove bag and then *in situ* transferred to a continuous He-flow optical cryostat.

Polarization-resolved Raman scattering measurements were performed in the quasibackscattering geometry. For excitation, we used Kr^+ ion laser lines with photon energies ranging from 1.55 to 3.05 eV. All spectra were acquired with 1800 grooves/mm diffraction gratings (spectral resolution ~ 0.1 meV) using a triple stage spectrometer setup.

The scattering polarization geometries used in this paper are labeled as e_i (e_s), where $e_{i(s)}$ denotes the polarization of the incident (collected) light. The incident and collected photons propagate along the c axis, with the polarization directed in plane. The energy of the incident (scattered) photons are denoted as $\omega_{i(s)}$. The four scattering polarization geometries used in this paper are XX, YX, RR, and RL. The linear light polarization directions, X and Y, lie within the ab plane and are orthogonal to one another. R and L denote right and left circularly polarized light, respectively, such that $R(L) = X \pm iY$.

Raman selection rules are listed in Table I. The bulk Raman excitations have either A_{1g} , A_{2g} , or E_g symmetry. The irreducible representations of the Raman-active phonons at the Γ point are $2A_{1g} + 2E_g$ [20–22]. In addition, there are four infrared (IR) active phonons, whose irreducible representations are $2A_{2u} + 2E_u$ [20].

In Fig. 1, we plot on semilog scale spectra of the Raman susceptibility for $\text{Bi}_2\text{Te}_{3-x}\text{Se}_x$. Measurements were performed in the XX scattering geometry at 15 K. The major spectral features are fitted to a Lorentzian function and overlaid with the experimental data to aid the reader's eye.

The Raman susceptibility was derived from the secondary emission spectra which contains both Raman and photoluminescence (PL) contributions. The measured secondary emission spectra, $S(\omega_i, \omega_s)$, differs from the Raman susceptibility, $\chi''(\omega)$, by two factors

$$S(\omega_i, \omega_s) \sim C(\omega_i, \omega_s) \{ [1 + n_B(\omega)] \chi''(\omega_i, \omega) + PL(\omega_i, \omega_s) \}, \quad (1)$$

where $n_B(\omega)$ is the Bose-Einstein distribution, $C(\omega_i, \omega_s)$ is a correction factor that accounts for the scattering volume and power loss due to the optical properties of the materials, and

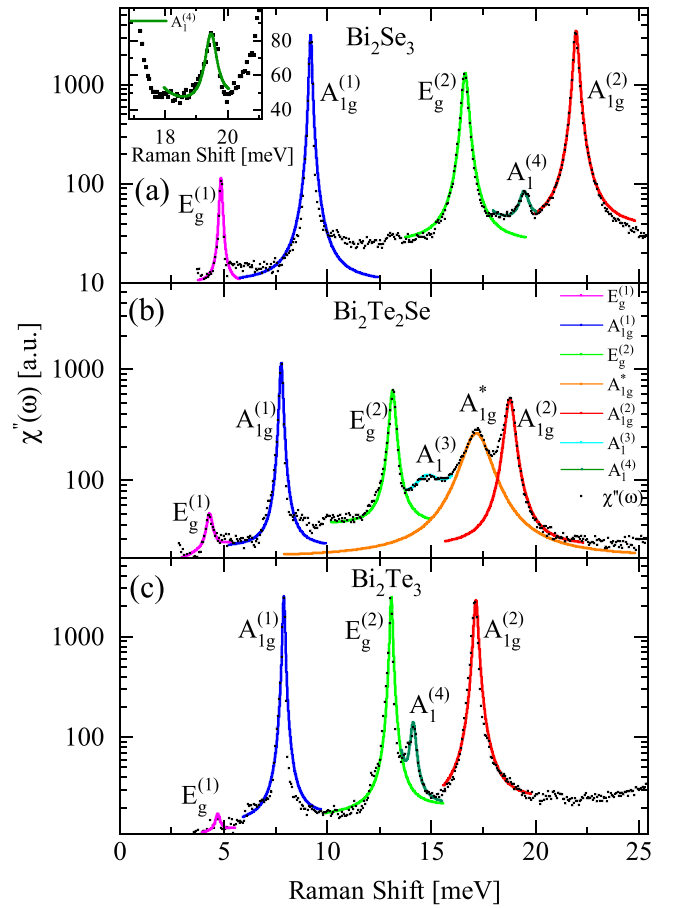


FIG. 1. Raman response spectra of $\text{Bi}_2\text{Te}_{3-x}\text{Se}_x$ in the XX scattering polarization geometry taken from (a) Bi_2Se_3 , (b) $\text{Bi}_2\text{Te}_2\text{Se}$, and (c) Bi_2Te_3 . (inset) Data from Bi_2Se_3 plotted against linear scale to illustrate signal-to-noise ratio. All measurements were performed at 15 K with $\omega_i = 1.92$ eV excitation. The bulk phonons are overlaid with a fit to Lorentzian lineshape over a local linear background for visual aid. The mode labeled A_{1g}^* is an antisite defect mode. The secondary emission spectra were normalized for wavelength dependent scattering volume, the attenuation in the sample, and reflectivity/transmission of light at the surface interface, see Eqs. (1) and (2), using optical data from Refs. [23–25]; then the Raman susceptibility was derived by subtracting the PL signal.

$PL(\omega_i, \omega_s)$ is the contribution from photoluminescence. The form of $C(\omega_i, \omega_s)$ for the backscattering geometry was derived in Refs. [26,27]

$$C(\omega_i, \omega_s) = \frac{\alpha(\omega_i) + \alpha(\omega_s)}{T(\omega_i)T(\omega_s)} n(\omega_s)^2, \quad (2)$$

where α is the optical extinction coefficient, T is the transmission coefficient at the crystal-vacuum interface, and $n(\omega_s)$ is the index of refraction of the material. The values of the optical properties of the $\text{Bi}_2\text{Te}_{3-x}\text{Se}_x$ crystals are taken from previously published data [23–25].

The Raman susceptibility spectra was derived from the renormalized secondary emission spectra by subtracting the PL contribution. The PL contribution to the secondary emission spectra is approximately a linear background in the narrow spectral range of the Raman excitations [19]. We

TABLE II. Summary of the bulk and surface mode energies in $\text{Bi}_2\text{Te}_2\text{Se}$ and Bi_2Te_3 . All values are given in units of meV.

Symmetry	$\text{Bi}_2\text{Te}_2\text{Se}$		Bi_2Te_3	
	This work	Literature	This work	Literature
$A_{1g}^{(1)}$	8.1	8.4 [28]	7.8	7.8 [20]
$A_{1g}^{(2)}$	19.1	19.6 [28]	17.2	16.6 [20]
$E_g^{(1)}$	4.5	4.3 [28]	4.7	4.4 [21]
$E_g^{(2)}$	13.5	13.7 [28]	13.1	12.8 [20]
$A_{2u}^{(1)}$		15.9 [29]		11.7 [20]
$A_{2u}^{(2)}$		17.1 [29]		14.9 [20]
$E_u^{(1)}$		7.7 [30]		6.2 [20]
				6.0 [15,21]
$E_u^{(2)}$		14.5 [28,31]		11.8 [20]
$A_1^{(1)}$	7.4		7.5	7.7 [32]
$A_1^{(2)}$			16.7	17.4 [32]
$A_1^{(3)}$	15.2	14.8 [33]	10.3	
$A_1^{(4)}$	16.7		14.0	14.1 [15]
				14.8 [32]
$E^{(1)}$	4.18			5.0 [32]
$E^{(2)}$	13.0		12.3	12.4 [32]
$E^{(3)}$	7.8		7.1	
$E^{(4)}$	14.9		12.3	

approximated the background to be the normalized spectral intensity 2.5 meV away from the laser excitation line, where the Raman continuum is still negligibly weak.

III. RESULTS AND DISCUSSION

The most prominent spectral features in the $\text{Bi}_2\text{Te}_{3-x}\text{Se}_x$ secondary emission spectra are the Raman-active bulk phonons. The energy of the modes are consistent with previously reported results, see Table II. In $\text{Bi}_2\text{Te}_2\text{Se}$, there is an additional broad mode, labeled A_{1g}^* , that is generally accepted to be the result of an antisite defect induced local vibration [33]. It should be noted that the bulk phonons consistently shift to higher energies with Se concentration, see Fig. 3(e).

In Fig. 2, we show the evolution of the energy and linewidth of the $A_{1g}^{(2)}$ mode in $\text{Bi}_2\text{Te}_{3-x}\text{Se}_x$ as a function of temperature. The $A_{1g}^{(2)}$ mode is used as an example of the other phonon modes, which display qualitatively similar behavior. The phonons are fit using the Voigt profile function to deconvolute the effects of the spectrometer resolution from the phonon linewidths. The energy and linewidth of the mode are fit to a two-phonon anharmonic decay model [34]:

$$\omega(T) = \omega_0 + \omega_R(2n_B(\omega_0/2, T) + 1), \quad (3)$$

$$\Gamma(T) = \Gamma_0 + \Gamma_R(2n_B(\omega_0/2, T) + 1), \quad (4)$$

where $\omega(T)$ and $\Gamma(T)$ are the energy and linewidth of the phonon at temperature T , ω_0 is the bare energy, Γ_0 is the residual linewidth, and ω_R and Γ_R are fitting parameters.

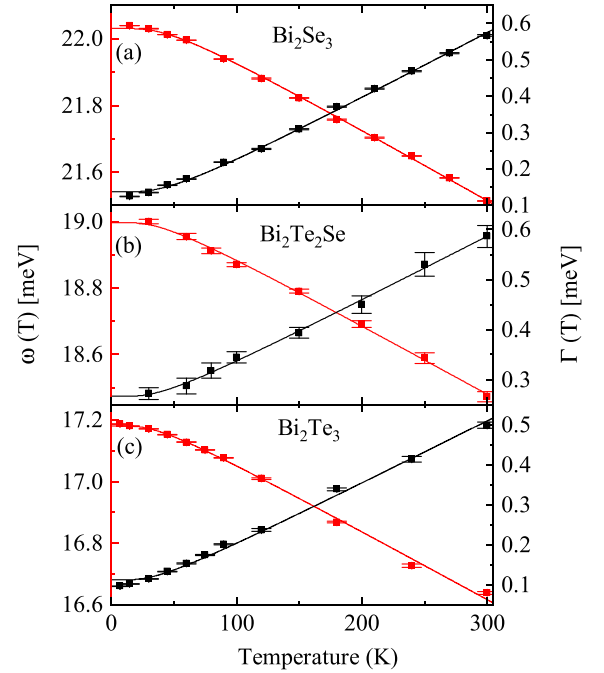


FIG. 2. Temperature dependence of the energy and linewidth of the $A_{1g}^{(2)}$ phonon mode of $\text{Bi}_2\text{Te}_{3-x}\text{Se}_x$. The energy (red) and linewidth (black) values of the $A_{1g}^{(2)}$ mode of (a) Bi_2Se_3 , (b) $\text{Bi}_2\text{Te}_2\text{Se}$, and (c) Bi_2Te_3 are displayed in units of meV. The temperature dependence of the energy and linewidth of the $A_{1g}^{(2)}$ mode is fit to a two-phonon anharmonic decay model [34].

The $A_{1g}^{(2)}$ mode is well described by the standard two-phonon anharmonic decay model, with residual linewidths consistent with previous temperature dependence measurements indicating good bulk crystal quality, see Table III.

The discontinuity of the crystal structure at the surface of $\text{Bi}_2\text{Te}_{3-x}\text{Se}_x$ has several important consequences. Since inversion symmetry is broken at the surface, the distinction between Raman and IR-active phonons is lifted and both types of modes are observable using the Raman probe. The optical phonons at the surface are described by the irreducible representations of the $\bar{\Gamma}$ point. By making the approximation that the crystal structure at the surface is comparable with the bulk crystal structure, the surface phonons are classified according to the corresponding bulk phonons they branch off from. Under this assumption, the irreducible representations of the optical surface phonons are $4A_1 + 4E$. In the notation used throughout this paper, $W^{(1,2)}$ refers to the Raman-related surface modes and $W^{(3,4)}$ refers to the IR-related surface modes, where $W = A_1$ or E ; for example, the surface mode counterparts of the $A_{2u}^{(1)}$ and $A_{2u}^{(2)}$ modes are $A_1^{(3)}$ and $A_1^{(4)}$. A

TABLE III. Residual linewidths Γ_0 for the $A_{1g}^{(2)}$ phonon modes. All values are given in units of meV.

Material	This work	Literature
Bi_2Se_3	0.08	0.06 [35]
$\text{Bi}_2\text{Te}_2\text{Se}$	0.20	0.39 [33]
Bi_2Te_3	0.07	0.09 [35]

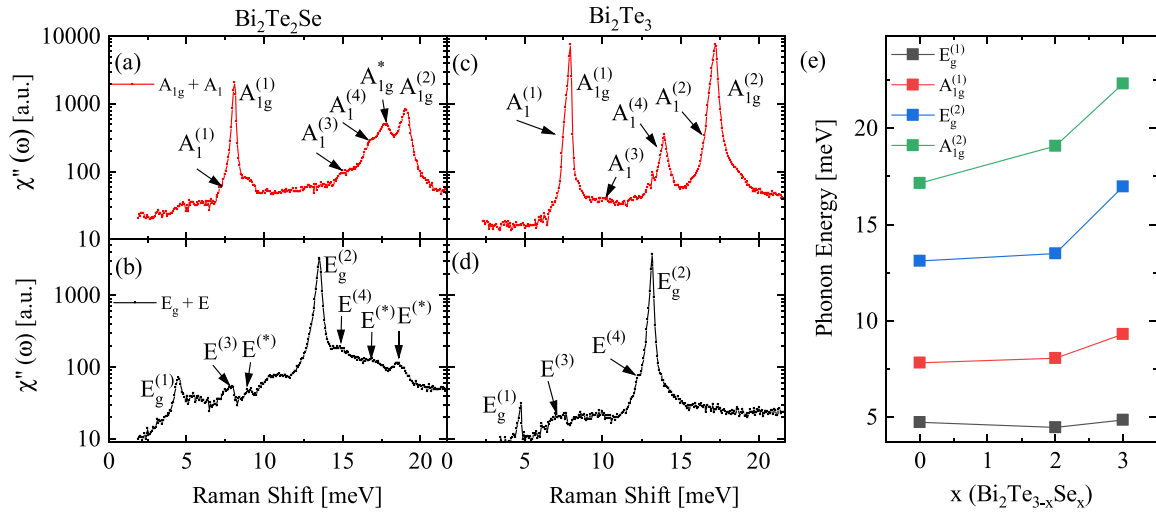


FIG. 3. High resolution $\chi''(\omega)$ spectra of $\text{Bi}_2\text{Te}_2\text{Se}$ and Bi_2Te_3 . $\chi''(\omega)$ spectra of $\text{Bi}_2\text{Te}_2\text{Se}$ are taken in the (a) RR and (b) RL scattering geometries. The modes labeled $E^{(*)}$ were previously reported [28], though their origin is unclear. $\chi''(\omega)$ spectra of Bi_2Te_3 are acquired in the (c) RR and (d) RL scattering geometries. In all cases, the spectra were acquired at 15 K with 1.92 eV excitation energy, and are plotted in semilog scale. (e) Phonon energy of $\text{Bi}_2\text{Te}_{3-x}\text{Se}_x$ as a function of Se concentration (x).

second important consequence is that the change in the crystal field potential at the surface will be reflected in the differences between the bulk and surface Raman spectra. For example, the energy and linewidth of the surface modes will shift relative to their bulk counterparts, indicating weaker or stronger bond strengths. Thus, information about the electronic/vibration properties at the surface may be inferred from the surface Raman spectra.

The most distinctive surface related features are the $A_1^{(3)}$ and $A_1^{(4)}$ surface phonons. In Bi_2Se_3 and Bi_2Te_3 , the $A_1^{(4)}$ mode is the strongest surface mode [14,15], whereas in $\text{Bi}_2\text{Te}_2\text{Se}$ the $A_1^{(3)}$ mode is the strongest. However, the majority of surface phonon modes are more than an order of magnitude weaker than their bulk counterparts, making their observation difficult. In order to aid their observation, we used polarization-resolved resonant Raman data to selectively probe the different irreducible representations. The previous Raman study used this method to identify the surface phonon modes in Bi_2Se_3 [14], therefore, we restrict our analysis to the surface phonons in Bi_2Te_3 and $\text{Bi}_2\text{Te}_2\text{Se}$.

In Figs. 3(a) and 3(b), we show the Raman response function of $\text{Bi}_2\text{Te}_2\text{Se}$ in the RR and RL scattering geometries, respectively. The $A_1^{(1)}$ mode (7.3 meV) is red shifted (~ 0.7 meV) from the $A_{1g}^{(1)}$ mode. The $A_1^{(2)}$ mode is obscured by the A_{1g}^* feature, and therefore cannot be detected by this method. The $E^{(1)}$ and $E^{(2)}$ modes are not sufficiently red shifted from their bulk counterparts to be detected. Lattice dynamics calculations of $\text{Bi}_2\text{Te}_2\text{Se}$ using density functional theory (DFT) [29] suggest that the A_1 features at 15.2 meV and 16.7 meV are the $A_1^{(3)}$ and $A_1^{(4)}$ modes, respectively. Similarly, the E features at 7.8 meV and 14.9 meV are the $E^{(3)}$ and $E^{(4)}$ modes, respectively [24,28,30,31]. In addition, we detected several vibrational modes with spectral intensities comparable to the surface phonons, labeled E^* , that were previously reported from IR spectroscopy measurements [28], though their origin remains unclear.

In Figs. 3(c) and 3(d), we show the Raman spectra of Bi_2Te_3 in the RR and RL scattering geometries, respectively. The $A_1^{(1)}$ (7.5 meV) and $A_1^{(2)}$ (16.7 meV) modes are red shifted from their A_{1g} counterparts by 0.3 meV and 0.5 meV, respectively. The $A_1^{(3)}$ (10.3 meV) and $A_1^{(4)}$ (14.0 meV) modes are red shifted from their IR counterparts by 1.4 meV and 0.9 meV, respectively [20]. Similar to the case of $\text{Bi}_2\text{Te}_2\text{Se}$, the $E^{(1)}$ and $E^{(2)}$ phonons are obscured by their bulk counterparts. The $E^{(3)}$ and $E^{(4)}$ surface modes appear at 7.1 meV and 12.3 meV, respectively.

The shifts in energy of the surface phonons relative to their bulk counterparts can be understood in the following way. The small red shifting of the A_1 modes is due to the lack of interlayer van der Waals restorative force on the vacuum side of the surface layer [36]. The lack of energy shifting by the E modes suggests that the surface termination does not significantly alter the in-plane bond dynamics. We may infer, based on the similar character of the surface phonons to their bulk counterparts, that the surface lattice dynamics of $\text{Bi}_2\text{Te}_{3-x}\text{Se}_x$ is nearly identical to the bulk. This is in stark contrast to conventional 3D materials where the surface termination radically alters the structural and chemical properties of the top-most atomic layers.

To further investigate the spectral characteristics of the surface and bulk phonons, we collected the data by varying excitation frequency ω_i . The relevant spectral characteristic of interest is the integrated intensity of a particular mode as a function of ω_i , $I_{ph}(\omega_i)$. The resonant enhancement factor of Raman active phonons is correlated to transitions between the initial and intermediate electronic states. Therefore, we may deduce the evolution of the electronic energy gaps in these materials by tracking $I_{ph}(\omega_i)$. Moreover, the Fano antiresonance effect on the surface phonons in Bi_2Se_3 [14,15] can be studied in greater detail as both the Raman coupling to the surface phonons and to the electronic continua is enhanced when incoming photon energy ω_i resonates with the

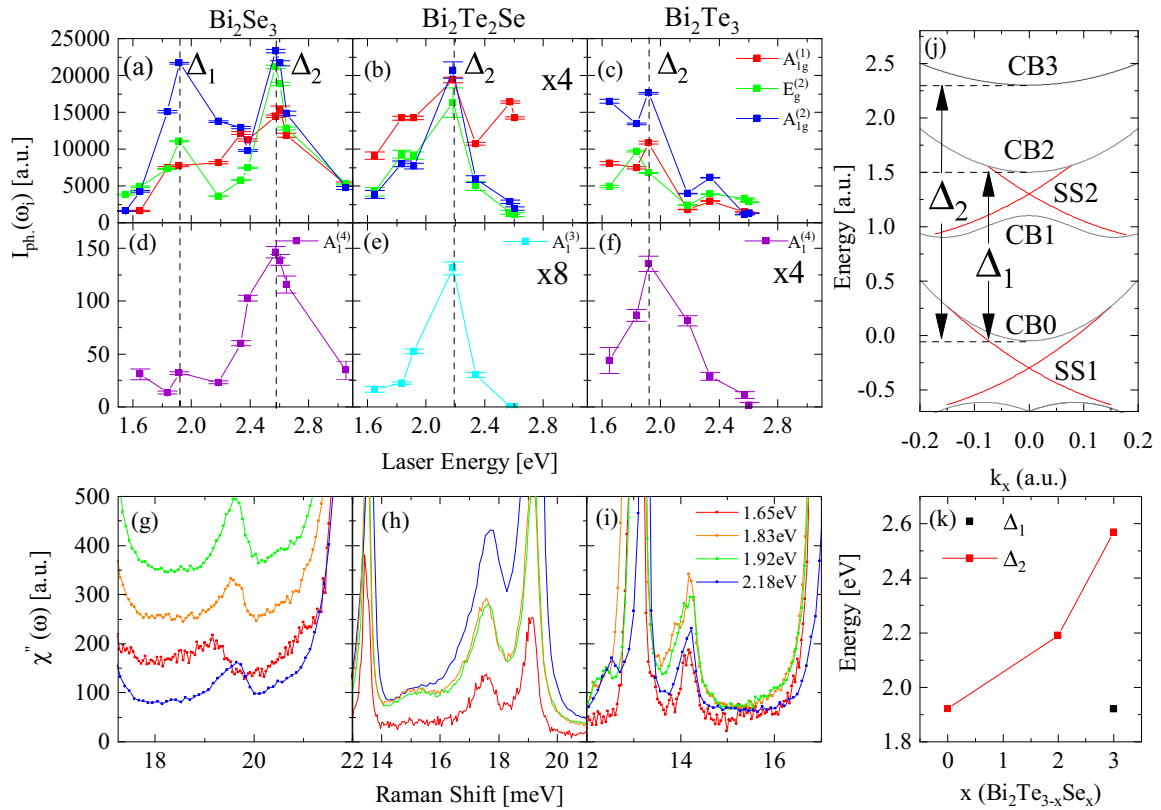


FIG. 4. Resonant Raman excitation profile (RREP) of the major low energy spectral features in $\text{Bi}_2\text{Te}_{3-x}\text{Se}_x$. (a)–(c) Integrated intensity of the major bulk phonons, and (d)–(f) the $A_1^{(3)}$ (Bi_2Se_3 and Bi_2Te_3) or $A_1^{(4)}$ ($\text{Bi}_2\text{Te}_2\text{Se}$) surface phonon plotted against excitation energy ω_i . The dotted vertical lines are to guide the reader’s eye. (g)–(i) Raman spectra for $\text{Bi}_2\text{Te}_{3-x}\text{Se}_x$ in the spectral region of the $A_1^{(3)}$ and $A_1^{(4)}$ surface phonons with optical corrections, see Eqs. (1) and (2). The PL signal was approximated to a linear background and subtracted accordingly. (j) Model of the electronic band structure near the Γ point for $\text{Bi}_2\text{Te}_{3-x}\text{Se}_x$. The lowest energy surface states (SS1), and unoccupied topological surface states (SS2) are depicted by red lines [13,18,19,37–39]. The bulk bands are shown in gray. (k) Evolution of the Δ_1 and Δ_2 energy gaps as a function of Se concentration (x).

energies of interband transitions. The surface phonons were fit using the local fits of the bulk phonons in closest in proximity.

In Fig. 4, we show the resonant Raman excitation profile (RREP) for the major spectral features in $\text{Bi}_2\text{Te}_{3-x}\text{Se}_x$ and the corresponding electronic band gaps that can be deduced from the peaks in $I_{ph}(\omega_i)$. In Figs. 4(a)–4(c), we show the $I_{ph}(\omega_i)$ for the $A_{1g}^{(1)}$, $A_{1g}^{(2)}$, and $E_g^{(2)}$ bulk phonon modes from $\omega_i = 1.65$ – 3.05 eV; the $E_g^{(1)}$ phonon mode is not included as its spectral intensity was insufficient for proper analysis. In Figs. 4(d)–4(f), we show the $I_{ph}(\omega_i)$ of either the $A_1^{(3)}$ or $A_1^{(4)}$ surface modes as the excitation profile of the other mode could not be determined. The dashed lines between the figures are meant to guide the reader’s eye. In Figs. 4(g)–4(i), we show Raman spectra for several excitations used in the RREP. The electronic band structure of $\text{Bi}_2\text{Te}_{3-x}\text{Se}_x$ near the Γ point is illustrated in Fig. 4(j) [40], with the corresponding values of the electronic band gaps Δ_1 and Δ_2 plotted in Fig. 4(k).

The RREPs of the phonon modes can be understood by considering the evolution of Δ_1 and Δ_2 with Se concentration. The two resonances in the excitation profile in Bi_2Se_3 at 1.9 eV and 2.6 eV correspond to the band gaps between CB0 and the third- and fourth-lowest conduction bands, CB2

and CB3, respectively [13,41]. In contrast, $\text{Bi}_2\text{Te}_2\text{Se}$ and Bi_2Te_3 only possess a single peak in their excitation profiles at ~ 2.2 eV and ~ 1.9 eV, respectively, corresponding to the Δ_2 band gap. This is because the Δ_1 band gap is smaller than 1.6 eV in these materials [13]. These results are consistent with previous excitation dependent measurements of Bi_2Se_3 and Bi_2Te_3 [15]. However, previous studies only employed three laser energies, making it difficult to find the resonance peak and further correlate the resonance factor to the band structure [42].

Finally, we determined the spectral properties of the electronic continuum that induces the Fano resonance of the $A_1^{(4)}$ surface mode of Bi_2Se_3 . When an electronic continuum interacts with a discrete phonon excitation, the Fano effect induces an asymmetrical spectral lineshape of the phonon [43,44]. The degree of asymmetry depends on several factors including the electron-phonon interaction strength v , the electronic density of states $\rho(\omega)$, the phonon-light-interaction strength t_{ph} , and the continuum-light-interaction strength t_e [44,45]. Therefore, one may extract information about the continuum by tracking the phonon lineshape as a function of excitation energy ω_i .

In principle, a surface phonon can couple to any electronic continuum with the same symmetry where the transitioning

electrons interact with the surface phonon. The “electronic continuum” in this case is the Raman continuum of electron-hole excitations that the surface phonon energy coincides with. The strength of the interaction depends on several factors; in the case of Bi_2Se_3 only a single continuum can couple to the $A_1^{(4)}$ mode. There are three low-energy electronic continua in Bi_2Se_3 : the intraband surface continuum of $\text{SS1}_- \rightarrow \text{SS1}_+$ transitions [where SS1_\pm refers to the upper (lower) branches of SS1], the interband surface-to-bulk continua of $\text{SS1}_- \rightarrow \text{CB0}$, and $\text{SS1}_+ \rightarrow \text{CB0}$ transitions continuum. Since the chemical potential crosses 150 meV above the Dirac point, the onset of the intraband surface continuum is roughly 300 meV, which is well above $A_1^{(4)}$ mode energy. The onset of the $\text{SS1}_- \rightarrow \text{CB0}$ continuum will be approximately 150 meV, with transitions between the Dirac point and the CB0 minimum [12]. Thus, the $A_1^{(4)}$ mode falls only within the $\text{SS1}_+ \rightarrow \text{CB0}$ continuum. Furthermore, if the $\text{SS1}_+ \rightarrow \text{CB0}$ continuum is selectively enhanced using resonant Raman scattering, then the effects of the other two continua are suppressed.

The lineshape of the Raman response for a phonon mode interacting with an electronic continuum, $\chi''(\omega)$, is described in the following way [14,27,44,45]:

$$\chi''(\omega) \sim \frac{t_e^2 \pi \rho (\omega_0 - \omega - vt_{ph}/t_e)^2}{(\omega - \omega_0)^2 + (\gamma - v^2 \rho \pi)^2}, \quad (5)$$

where t_{ph} and t_e denotes the vertices for the light scattering processes, v is the electron-phonon interaction, ω_0 is the bare phonon frequency, γ is the phonon half-width at half-maximum, and ρ is the density of the relevant continuum states. In Eq. (5), we have assumed that t_e and v are frequency independent constants for the given continuum. We have also neglected the real part of the electronic self-energy and assumed that $v^2 \rho \gg \gamma$ [14].

To determine the spectral properties of the $\text{SS1}_+ \rightarrow \text{CB0}$ transition, we fit the $A_1^{(4)}$ mode Raman spectra taken with different ω_i using Eq. (5), where ω_0 , γ , v , and ρ are assumed to be ω_i -independent constants. The factor t_e strongly depends on ω_i as it undergoes enhancement via the resonant Raman process through $\text{SS1} \rightarrow \text{SS2}$ dipole transitions.

In Fig. 5(a), we display fits to the $A_1^{(4)}$ surface mode data in Bi_2Se_3 for $\omega_i = 1.55$ – 2.65 eV excitations. The fits capture the strong Fano lineshape of the mode in the proximity of $\omega_i = 1.65$ eV excitation, the reduction of the mode’s asymmetry away from the resonance, and the excitation dependence of the phonon-light interaction strength. We obtain electron-phonon interaction strength $v = 0.28$ meV, which is similar to the value from earlier study [14] (0.32 meV).

In Fig. 5(b), we show the evolution of t_e^2 and t_{ph}^2 with excitation energy ω_i . There are two resonances in the t_e^2 profile: one at $\omega_i = 1.65$ eV due to SS1 - SS2 transitions, and another at $\omega_i = 2.5$ eV due to SS1 - CB3 transitions. Similarly, in the t_{ph}^2 profile there is a weak resonance at 1.83 eV and a stronger resonance at 2.55 eV. The onset of the SS1 - SS2 transitions is slightly below the Δ_1 transition, which is consistent with the model of the band structure [Fig. 4(j)]. The offset between the lower energy phononic and electronic resonances is likely because the surface phonon couples stronger to SS1 - CB2 transitions than to SS1 - SS2 transitions. The pronounced Fano lineshape of the $A_1^{(4)}$ surface mode at $\omega_i = 1.65$ eV is the

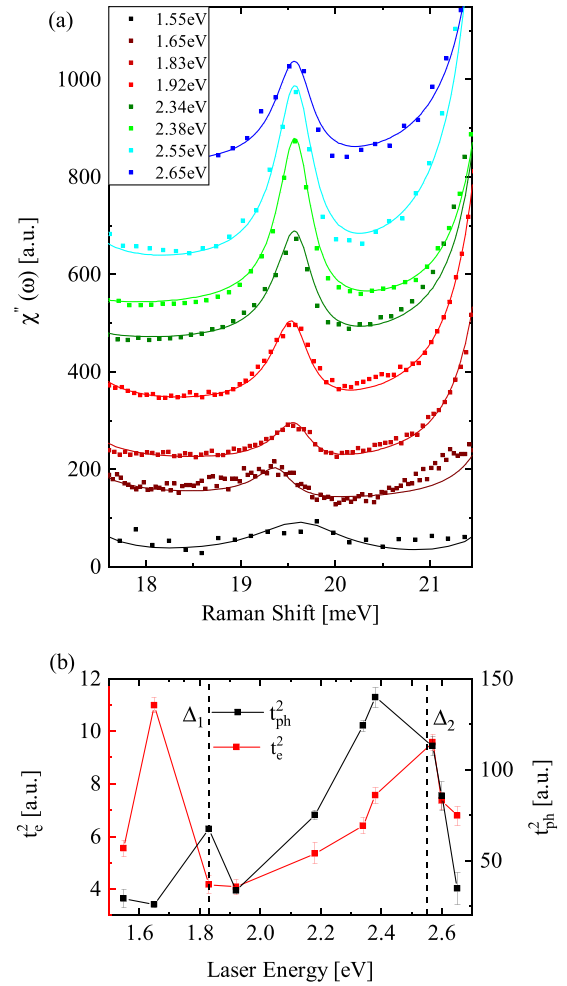


FIG. 5. Fano resonance profile of Bi_2Se_3 (a) Fano resonance of the $A_1^{(4)}$ surface phonon in Bi_2Se_3 for different ω_i . The data is shifted by a constant for each spectra for readability. (b) t_e^2 and t_{ph}^2 as a function of excitation energy ω_i . Values are derived from the fit to the Fano lineshape. The dotted vertical lines represent Δ_1 and Δ_2 energies, see Fig. 4(j).

result of the strong resonance in t_e^2 and the relatively weak resonance in t_{ph}^2 at this energy. Similarly, the $A_1^{(4)}$ surface mode develops a more Lorentzian lineshape at $\omega_i = 2.5$ eV due to the broader and weaker resonance in t_e^2 and the strong resonance in t_{ph}^2 at this energy.

IV. CONCLUSIONS

In conclusion, we have probed the surface phonons and the continuum of electronic transitions between surface conduction bands in $\text{Bi}_2\text{Te}_{3-x}\text{Se}_x$ using resonant Raman spectroscopy. By using polarization-resolved resonant Raman spectroscopy, we observed the surface counterparts of the bulk IR active phonons and the A_1 Raman surface phonons in all three materials. The surface counterparts of the bulk Raman active E_g phonons were not sufficiently red shifted to be resolved for adequate analysis. We determined that the energies of all phonon modes consistently harden with increased Se

concentration. In Bi_2Se_3 , the $A_1^{(4)}$ surface phonon undergoes a strong Fano antiresonance when the principal surface bands resonate with the next-lowest surface bands. This effect is not observed in $\text{Bi}_2\text{Te}_2\text{Se}$ or Bi_2Te_3 as the band gap in these materials is below the lowest laser energy of our setup. The quantitative similarities between the resonance profiles of the bulk and surface phonon modes is good evidence that the surface modes in these materials are related to the corresponding bulk phonons with renormalized energies due to their surface discontinuity.

ACKNOWLEDGMENTS

We thank R. Merlin and I. Boulares for discussions. The spectroscopic work (A.C.L., H.-H.K., and G.B.) was supported by the NSF under Grant No. DMR-2105001. The sample growth (X.W. and S.-W.C.) was supported by the DOE under Grant No. DE-FG02-07ER46382. The work at NICPB was supported by the European Research Council (ERC) under the European Union's Horizon 2020 research and innovation programme Grant Agreement No. 885413.

- [1] J. E. Moore, The birth of topological insulators, *Nature (London)* **464**, 194 (2010).
- [2] M. Z. Hasan and C. L. Kane, Colloquium: Topological insulators, *Rev. Mod. Phys.* **82**, 3045 (2010).
- [3] L. Fu, C. L. Kane, and E. J. Mele, Topological insulators in three dimensions, *Phys. Rev. Lett.* **98**, 106803 (2007).
- [4] P. Roushan, J. Seo, C. V. Parker, Y. S. Hor, D. Hsieh, D. Qian, A. Richardella, M. Z. Hasan, R. J. Cava, and A. Yazdani, Topological surface states protected from backscattering by chiral spin texture, *Nature (London)* **460**, 1106 (2009).
- [5] I. Žutić, J. Fabian, and S. Das Sarma, Spintronics: Fundamentals and applications, *Rev. Mod. Phys.* **76**, 323 (2004).
- [6] J. Linder, T. Yokoyama, and A. Sudbø, Anomalous finite size effects on surface states in the topological insulator Bi_2Se_3 , *Phys. Rev. B* **80**, 205401 (2009).
- [7] S. R. Park, W. S. Jung, C. Kim, D. J. Song, C. Kim, S. Kimura, K. D. Lee, and N. Hur, Quasiparticle scattering and the protected nature of the topological states in a parent topological insulator Bi_2Se_3 , *Phys. Rev. B* **81**, 041405(R) (2010).
- [8] S. Nakajima, The crystal structure of $\text{Bi}_2\text{Te}_{3-x}\text{Se}_x$, *J. Phys. Chem. Solids* **24**, 479 (1963).
- [9] A. Ribak, K. B. Chashka, E. Lahoud, M. Naamneh, S. Rinott, Y. Ein-Eli, N. C. Plumb, M. Shi, E. Rienks, and A. Kanigel, Internal pressure in superconducting Cu-intercalated Bi_2Se_3 , *Phys. Rev. B* **93**, 064505 (2016).
- [10] T. Arakane, T. Sato, S. Souma, K. Kosaka, K. Nakayama, M. Komatsu, T. Takahashi, Z. Ren, K. Segawa, and Y. Ando, Tunable Dirac cone in the topological insulator $\text{Bi}_{2-x}\text{Sb}_x\text{Te}_{3-y}\text{Se}_y$, *Nat. Commun.* **3**, 636 (2012).
- [11] Y. L. Chen, J. G. Analytis, J.-H. Chu, Z. K. Liu, S.-K. Mo, X. L. Qi, H. J. Zhang, D. H. Lu, X. Dai, Z. Fang, S. C. Zhang, I. R. Fisher, Z. Hussain, and Z.-X. Shen, Experimental realization of a three-dimensional topological insulator, Bi_2Te_3 , *Science* **325**, 178 (2009).
- [12] Y. Xia, D. Qian, D. Hsieh, L. Wray, A. Pal, H. Lin, A. Bansil, D. Grauer, Y. S. Hor, R. J. Cava *et al.*, Observation of a large-gap topological-insulator class with a single Dirac cone on the surface, *Nat. Phys.* **5**, 398 (2009).
- [13] D. Niesner, T. Fauster, S. V. Eremeev, T. V. Menshchikova, Y. M. Koroteev, A. P. Protogenov, E. V. Chulkov, O. E. Tereshchenko, K. A. Kokh, O. Alekperov, A. Nadjafov, and N. Mamedov, Unoccupied topological states on bismuth chalcogenides, *Phys. Rev. B* **86**, 205403 (2012).
- [14] H.-H. Kung, M. Salehi, I. Boulares, A. F. Kemper, N. Koirala, M. Brahlek, P. Lošťák, C. Uher, R. Merlin, X. Wang, S.-W. Cheong, S. Oh, and G. Blumberg, Surface vibrational modes of the topological insulator Bi_2Se_3 observed by Raman spectroscopy, *Phys. Rev. B* **95**, 245406 (2017).
- [15] I. Boulares, G. Shi, E. Kioupakis, P. Lošťák, C. Uher, and R. Merlin, Surface phonons in the topological insulators Bi_2Se_3 and Bi_2Te_3 , *Solid State Commun.* **271**, 1 (2018).
- [16] J. Dai, D. West, X. Wang, Y. Wang, D. Kwok, S.-W. Cheong, S. B. Zhang, and W. Wu, Toward the intrinsic limit of the topological insulator Bi_2Se_3 , *Phys. Rev. Lett.* **117**, 106401 (2016).
- [17] L.-L. Wang, M. Huang, S. Thimmaiah, A. Alam, S. L. Bud'ko, A. Kaminski, T. A. Lograsso, P. Canfield, and D. D. Johnson, Native defects in tetradymite $\text{Bi}_2(\text{Te}_x\text{Se}_{3-x})$ topological insulators, *Phys. Rev. B* **87**, 125303 (2013).
- [18] H.-H. Kung, S. Maiti, X. Wang, S.-W. Cheong, D. L. Maslov, and G. Blumberg, Chiral spin mode on the surface of a topological insulator, *Phys. Rev. Lett.* **119**, 136802 (2017).
- [19] H.-H. Kung, A. P. Goyal, D. L. Maslov, X. Wang, A. Lee, A. F. Kemper, S.-W. Cheong, and G. Blumberg, Observation of chiral surface excitons in a topological insulator Bi_2Se_3 , *Proc. Natl. Acad. Sci. USA* **116**, 4006 (2019).
- [20] W. Richter and C. Becker, A Raman and far-infrared investigation of phonons in the rhombohedral V2–VI3 compounds Bi_2Te_3 , Bi_2Se_3 , Sb_2Te_3 and $\text{Bi}_2(\text{Te}_{1-x}\text{Se}_x)_3$ ($0 < x < 1$), $(\text{Bi}_{1-y}\text{Sb}_y)_2\text{Te}_3$ ($0 < y < 1$), *Phys. Stat. Sol. (b)* **84**, 619 (1977).
- [21] B.-T. Wang and P. Zhang, Phonon spectrum and bonding properties of Bi_2Se_3 : Role of strong spin-orbit interaction, *Appl. Phys. Lett.* **100**, 082109 (2012).
- [22] W. Cheng and S.-F. Ren, Phonons of single quintuple Bi_2Te_3 and Bi_2Se_3 films and bulk materials, *Phys. Rev. B* **83**, 094301 (2011).
- [23] J. W. McIver, D. Hsieh, S. G. Drapcho, D. H. Torchinsky, D. R. Gardner, Y. S. Lee, and N. Gedik, Theoretical and experimental study of second harmonic generation from the surface of the topological insulator Bi_2Se_3 , *Phys. Rev. B* **86**, 035327 (2012).
- [24] Y. A. Aleshchenko, A. V. Muratov, V. V. Pavlova, Y. G. Selivanov, and E. G. Chizhevskii, Infrared spectroscopy of $\text{Bi}_2\text{Te}_2\text{Se}$, *JETP Lett.* **99**, 187 (2014).
- [25] H. Cui, I. Bhat, and R. Venkatasubramanian, Optical constants of Bi_2Te_3 and Sb_2Te_3 measured using spectroscopic ellipsometry, *J. Electron. Mater.* **28**, 1111 (1999).
- [26] R. Loudon, Theory of the resonance Raman effect in crystals, *Journal de Physique* **26**, 677 (1965).
- [27] G. Blumberg, M. Klein, L. Börjesson, R. Liang, and W. Hardy, Investigation of the temperature dependence of electron and

- phonon Raman scattering in single crystal $\text{YBa}_2\text{Cu}_3\text{O}_{6.952}$, *J. Supercond.* **7**, 445 (1994).
- [28] A. Akrap, M. Tran, A. Ubaldini, J. Teyssier, E. Giannini, D. van der Marel, P. Lerch, and C. C. Homes, Optical properties of $\text{Bi}_2\text{Te}_2\text{Se}$ at ambient and high pressures, *Phys. Rev. B* **86**, 235207 (2012).
- [29] H. Shi, D. Parker, M.-H. Du, and D. J. Singh, Connecting thermoelectric performance and topological-insulator behavior: Bi_2Te_3 and $\text{Bi}_2\text{Te}_2\text{Se}$ from first principles, *Phys. Rev. Appl.* **3**, 014004 (2015).
- [30] A. A. Reijnders, Y. Tian, L. J. Sandilands, G. Pohl, I. D. Kivlichan, S. Y. F. Zhao, S. Jia, M. E. Charles, R. J. Cava, N. Alidoust, S. Xu, M. Neupane, M. Z. Hasan, X. Wang, S. W. Cheong, and K. S. Burch, Optical evidence of surface state suppression in Bi-based topological insulators, *Phys. Rev. B* **89**, 075138 (2014).
- [31] P. Di Pietro, F. M. Vitucci, D. Nicoletti, L. Baldassarre, P. Calvani, R. Cava, Y. S. Hor, U. Schade, and S. Lupi, Optical conductivity of bismuth-based topological insulators, *Phys. Rev. B* **86**, 045439 (2012).
- [32] L. Ren, X. Qi, Y. Liu, G. Hao, Z. Huang, X. Zou, L. Yang, J. Li, and J. Zhong, Large-scale production of ultrathin topological insulator bismuth telluride nanosheets by a hydrothermal intercalation and exfoliation route, *J. Mater. Chem.* **22**, 4921 (2012).
- [33] Y. Tian, G. B. Osterhoudt, S. Jia, R. J. Cava, and K. S. Burch, Local phonon mode in thermoelectric $\text{Bi}_2\text{Te}_2\text{Se}$ from charge neutral antisites, *Appl. Phys. Lett.* **108**, 041911 (2016).
- [34] P. G. Klemens, Anharmonic decay of optical phonons, *Phys. Rev.* **148**, 845 (1966).
- [35] Y. Tian, S. Jia, R. J. Cava, R. Zhong, J. Schneeloch, G. Gu, and K. S. Burch, Understanding the evolution of anomalous anharmonicity in $\text{Bi}_2\text{Te}_{3-x}\text{Se}_x$, *Phys. Rev. B* **95**, 094104 (2017).
- [36] J. Zhang, Z. Peng, A. Soni, Y. Zhao, Y. Xiong, B. Peng, J. Wang, M. S. Dresselhaus, and Q. Xiong, Raman spectroscopy of few-quintuple layer topological insulator Bi_2Se_3 nanoplatelets, *Nano Lett.* **11**, 2407 (2011).
- [37] H. Soifer, A. Gauthier, A. F. Kemper, C. R. Rotundu, S.-L. Yang, H. Xiong, D. Lu, M. Hashimoto, P. S. Kirchmann, J. A. Sobota, and Z.-X. Shen, Band-resolved imaging of photocurrent in a topological insulator, *Phys. Rev. Lett.* **122**, 167401 (2019).
- [38] S. Eremeev, I. Silkin, T. Menshchikova, A. P. Protogenov, and E. V. Chulkov, New topological surface state in layered topological insulators: Unoccupied Dirac cone, *JETP Lett.* **96**, 780 (2013).
- [39] M. Nurmamat, E. E. Krasovskii, K. Kuroda, M. Ye, K. Miyamoto, M. Nakatake, T. Okuda, H. Namatame, M. Taniguchi, E. V. Chulkov, K. A. Kokh, O. E. Tereshchenko, and A. Kimura, Unoccupied topological surface state in $\text{Bi}_2\text{Te}_2\text{Se}$, *Phys. Rev. B* **88**, 081301(R) (2013).
- [40] H. Zhang, C.-X. Liu, X.-L. Qi, X. Dai, Z. Fang, and S.-C. Zhang, Topological insulators in Bi_2Se_3 , Bi_2Te_3 and Sb_2Te_3 with a single Dirac cone on the surface, *Nat. Phys.* **5**, 438 (2009).
- [41] J. A. Sobota, S.-L. Yang, A. F. Kemper, J. J. Lee, F. T. Schmitt, W. Li, R. G. Moore, J. G. Analytis, I. R. Fisher, P. S. Kirchmann, T. P. Devereaux, and Z.-X. Shen, Direct optical coupling to an unoccupied dirac surface state in the topological insulator Bi_2Se_3 , *Phys. Rev. Lett.* **111**, 136802 (2013).
- [42] W. H. Weber and R. Merlin, *Raman Scattering in Materials Science* (Springer Science & Business Media, 2000), Vol. 42, Chap. 1.2
- [43] U. Fano, Effects of configuration interaction on intensities and phase shifts, *Phys. Rev.* **124**, 1866 (1961).
- [44] M. V. Klein, Electronic Raman scattering, in *Light Scattering in Solids I*, edited by M. Cardona (Springer-Verlag, Berlin, 1983), pp. 147–204.
- [45] S.-F. Wu, W.-L. Zhang, L. Li, H.-B. Cao, H.-H. Kung, A. S. Sefat, H. Ding, P. Richard, and G. Blumberg, Coupling of fully symmetric As phonon to magnetism in $\text{Ba}(\text{Fe}_{1-x}\text{Au}_x)_2\text{As}_2$, *Phys. Rev. B* **102**, 014501 (2020).